Chapter 4

Metamaterial Antennas for Wireless Communications Transceivers

Mohammad Alibakhshikenari,
Mohammad Naser-Moghadasi,
Ramazan Ali Sadeghzadeh, Bal Singh Virdee and
Ernesto Limiti

Additional information is available at the end of the chapter

http://dx.doi.org/10.5772/66379

Abstract

Limited space is given to antennas in modern portable wireless systems, which means that antennas need to be small in size and compact structures. However, shrinkage of conventional antennas leads to performance degradation and complex mechanical assembly. Therefore, the design of miniature antennas for application in wireless communication systems is highly challenging using traditional means. In this chapter, it is shown that metamaterial (MTM) technology offers a solution to synthesize antennas with a small footprint with the added advantage of low cost and excellent radiation characteristics.

Keywords: antennas, ultra-wideband, metamaterials, composite right-/left-hand transmission lines, microstrip

1. Introduction

In this chapter, novel and compact planar antennas are presented including ultra-wideband (UWB) and hexa-band antennas. The UWB antenna presented in part 2 is based on metamaterial (MTM) transmission lines. In reality, the MTM antenna structure is more accurately described as a composite right-/left-handed transmission line (CRLH-TL) structure due to the resulting parasitic capacitance and inductance effects. The design of the UWB antenna is achieved by embedding E-shaped dielectric slits in the radiating patches. It is shown that the dimensions of such patches have a considerable influence on the radiation characteristics of the antenna. Parametric study is undertaken to demonstrate how the MTM unit-cell's parameters

affect the antennas performance in terms of gain, radiation efficiency, and radiation patterns. A novel antenna structure referred to as 'hexa-band' coplanar waveguide (CPW)-fed antenna, which is presented in part 3, consists of asymmetric fork-shaped-radiating elements incorporating U-shaped radiators with a slit. Each of the branched radiators generates triple resonant frequencies within the L-, S-, C- and X-bands.

2. Ultra-wideband antenna

Geometry of an innovative ultra-wideband (UWB) antenna in **Figure 1** shows that it is essentially a patch antenna with a rectangular slot. The antenna is terminated on the right-hand (RH) side with a grounded 50-Ω resistive load in order to reduce any impedance mismatch and thereby enhance the antenna's performance. Enclosed inside the slot are three radiating patches on which is etched an E-shaped dielectric slit. The middle patch of the antenna is excited through a coplanar waveguide (CPW) transmission line. A larger E-shaped slit is included in the antenna next to the 50-Ω load, which exhibits characteristics of the simplified composite right-/left-handed transmission line (SCRLH-TL) [1]. In the equivalent circuit of the antenna, the left-handed capacitance (C_L) results from the dielectric gap between the patches and the conductor next to the larger E-shaped slit. The impedance bandwidth of the antenna is affected by the smaller E-shaped slits and the dielectric gap represented by (C_L). In fact, the radiation properties of the antenna are affected by the dimensions of the three patches. Prototype of the antenna was fabricated on RT/duroid® RO4003 dielectric substrate, with a thickness (h) of 0.8 mm, dielectric constant (ε_r) of 3.38 and tanδ of 22×10^{-4}. The antenna design was optimized using full-wave electromagnetic (EM) simulators, that is, of Agilent Advanced Design System (ADS), High-Frequency Structure Simulator (HFSS™) and CST Microwave Studio (CST-MWS). The simulation results were validated with the actual measurements.

The configuration of the E-shaped slit was determined through simulation analysis. As it will be shown later, the size of the three patches actually has an influence of the antenna gain and efficiency properties. The equivalent circuit of the E-shaped slit with the absence of left-handed inductance (L_L) and its microstrip structure is shown in **Figure 2(a)** and **(b)**, respectively. Parameters of the simplified CRLH structure in **Figure 2** are given by

$$L(nH) = 0.2l\left[In\left(\frac{l}{W+l}\right) + 1.193 + \frac{W+l}{3l}\right] \times \left(0.57 - 0.145ln\frac{W}{h}\right) \quad (1a)$$

$$C(pF) = 10\,l\left[\frac{\sqrt{\varepsilon_e}}{Z_0} - \frac{\varepsilon_r W}{360\,\pi h}\right] \quad (1b)$$

$$\varepsilon_e = \frac{\varepsilon_r + 1}{2} + \frac{\varepsilon_r - 1}{2}\sqrt{\frac{1}{(1 + 10h/W)}} \quad (2)$$

where W and l represent the width and length of the microstrip line, respectively, and h and ε_r the thickness and relative permittivity of the substrate, respectively.

The E-shaped slit structure employed here is shown in **Figure 2(b)**. Based on the resonance frequencies of this structure, the initial magnitude of C_L, C_R, and L_R can be obtained from the dispersion relation of the SCRLH-TL. This is determined by applying the periodic boundary conditions related to the Bloch-Floquet theorem, given by

$$\varnothing(\omega) = \beta(\omega)p = cos^{-1}(1 + 1/ZY) \quad (3)$$

http://dx.doi.org/10.5772/66379

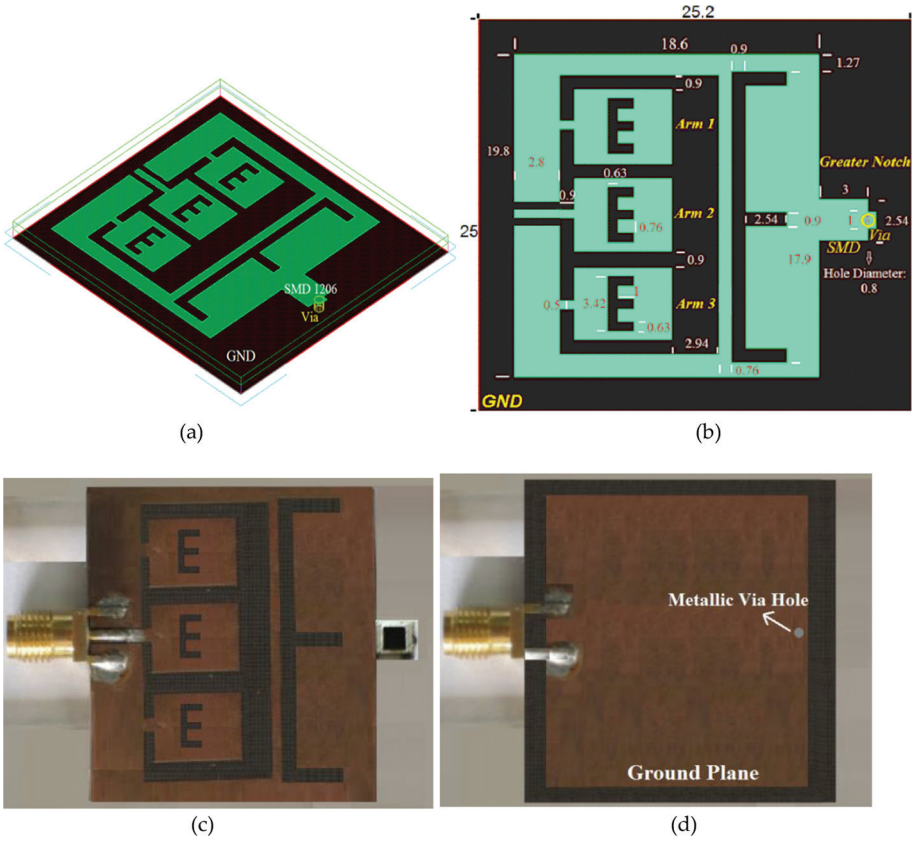

Figure 1. Test antenna prototype: (a) isometric view, (b) top view with dimensions annotated in millimetres, (c) top view of fabricated antenna and (d) bottom view of fabricated antenna.

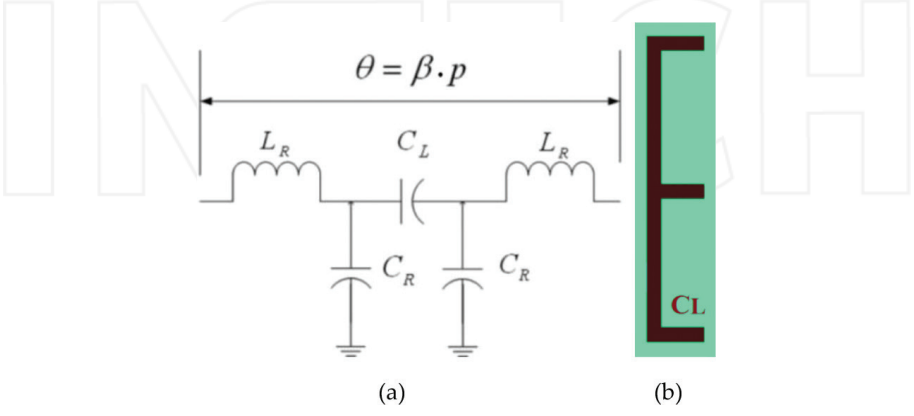

Figure 2. Simplified CRLH structure without inductance L_L: (a) lumped structure and (b) distributed equivalent one.

$$Z(\omega) = j(\omega L_R - 1/\omega C_L) \tag{4}$$

$$Y(\omega) = j\left(\omega C_R - 1/\omega L_L\right) \xrightarrow{\text{SCRLH-TL without } C_L \text{ or } L_L \text{ Here, without } L_L} Y(\omega) = j\omega C_R \tag{5}$$

The series impedance of the unit cell is represented by Z and its shunt admittance by Y. The series right-handed (RH) inductance is represented by L_R, and its shunt RH capacitance by C_R. By substituting Eqs. (4) and (5) into Eq. (3), the dispersion can be represented by

$$\varnothing(\omega) = cos^{-1}\left[1 - \left(\frac{C_R}{2C_L}\left(\omega^2 C_L L_R - 1\right)\right)\right] \tag{6}$$

Figure 3 shows the dispersion diagram of the antenna based on SCRLH-TL as determined by HFSS using Eq. (6).

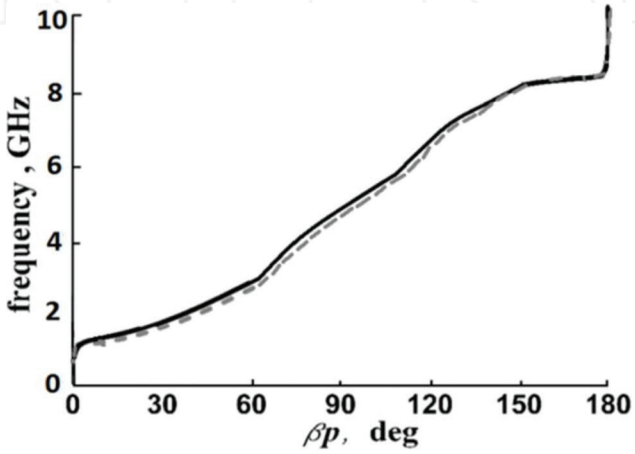

Figure 3. Dispersion diagram of the proposed antenna constructed using SCRLH-TL. HFSS™ (solid line) and Eq. (6) (dashed line).

Negative-order modes in the SCRLH-TL structure vanish with the absence of left-handed capacitance or inductance. Hence, the electrical size of the SCRLH-TL structure can be reduced by increasing the magnitude of C_L, L_R and C_R. This can be achieved by adjusting the structure dimensions. An optimization technique has been adopted within ADS, HFSS™ and CST-MWS commercial tools, leading to the final size of the structure. The resulting antenna dimensions are annotated in **Figure 1**, and the corresponding values of the lumped elements are $C_L = 8.2\ pF$, $L_R = 5.8\ nH$ and $C_R = 5.1\ pF$.

The antenna was fabricated using standard manufacturing techniques, and its performance measured. The physical dimensions of the antenna are $21.6 \times 19.8 \times 0.8\ mm^3$, and the corresponding electrical dimensions at 0.7 and 8 GHz, respectively, are $504 \times 10^{-4}\ \lambda_o \times 462 \times 10^{-4}\ \lambda_o \times 18 \times 10^{-4}\ \lambda_o$ and $576 \times 10^{-3}\ \lambda_o \times 528 \times 10^{-3}\ \lambda_o \times 21 \times 10^{-3}\ \lambda_o$, where λ_o is free-space wavelength. The ground-plane size of the antenna is $25.2 \times 25\ mm^2$.

http://dx.doi.org/10.5772/66379

Anechoic chamber was used to accurately characterize the antenna's performance in terms of its gain and radiation efficiency. This involved applying RF power to the antenna and measuring the EM field radiated from it in the surrounding space. Radiation efficiency was calculated by taking the ratio of the radiated power to the input power of the antenna. Standard gain comparison technique was used to measure the antenna's gain. This involved using a pre-calibrated standard gain antenna to find the absolute gain of the antenna under test.

Figure 4 shows how the vertical dielectric gap between small patches (L_{gap}), and the horizontal gap between small patches and the metallization next to the larger E-shaped slit (W_{gap}), affects the antenna's return-loss performance. It is evident from the simulation that both these dielectric gaps can have a significant effect on the impedance bandwidth of the antenna. The simulation results show that by reducing these gaps, the antenna's impedance bandwidth can be enhanced.

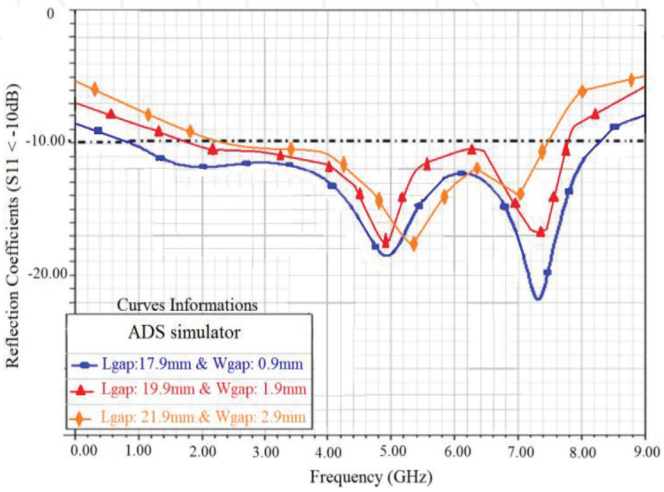

Figure 4. Effect of the gap between the three patches (L_{gap}) and the outer conductor (W_{gap}) adjacent to the larger E-shaped slit on the antenna impedance bandwidth.

Figure 5 shows the proposed antenna's measured and simulation return-loss performance, where the impedance bandwidth is defined by $S_{11} \leq$-10 dB. For comparison purposes, various EM simulation tools were employed to compute the impedance bandwidth of the antenna. Both HFSS™ and CST Microwave Studio (MWS) are powerful three-dimensional (3D) EM simulators, where HFSS™ is based on finite element method (FEM) technique and CST MWS is based upon finite integration technique. ADS is 2.5D EM tool based upon method of moment (MoM) technique. The impedance bandwidth predicted by the following: (1) ADS is 7.44 GHz (0.8–8.24 GHz); (2) CST MWS is 7.88 GHz (0.4–8.28 GHz) and (3) HFSS™ is 7.65 GHz (0.55– 8.2 GHz). The correlation between HFSS™ and CST-MWS is excellent. The measured fractional bandwidth is 167.8%, and the simulated fractional bandwidths are 164.6% (ADS), 181.6%, (CST-MWS) and 174.9% (HFSS™). The measured impedance bandwidth is 7.3 GHz (0.7–8 GHz). This confirms that the antenna can operate over an ultra-wideband.

The antenna resonates at two distinct frequencies, as shown in **Figure 5**, which are measured at 4.75 and 7 GHz. Simulation results predict 4.15 and 6.8 GHz (ADS), 4.03 and 6.68 GHz (CST-MWS), and 4 and 6.6 GHz (HFSS™). The measured results agree well with the ADS prediction. The divergence in the results is attributed to manufacturing tolerances.

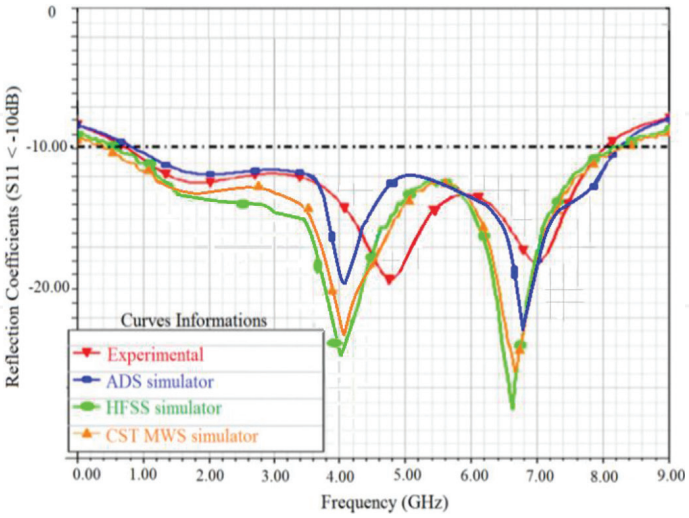

Figure 5. Antenna measured and simulated reflection coefficient response.

The distribution of the current density over the surface of the antenna at the two resonance frequencies of 4.75 and 7 GHz is shown in **Figure 6**. The current density distribution is symmetrical with reference to the feed line.

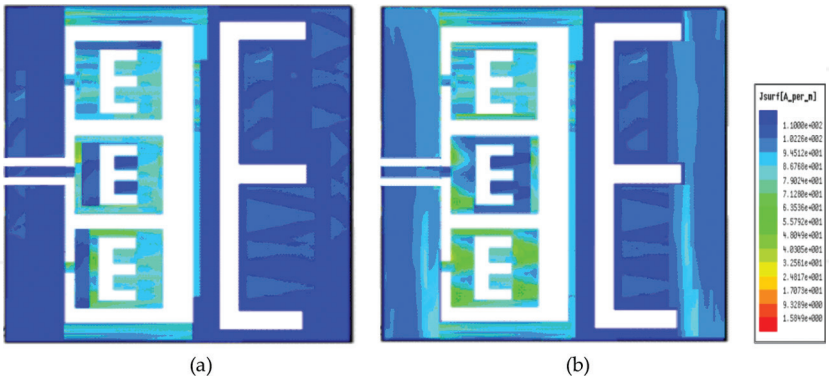

Figure 6. Current density distribution over the antenna at (a) 4.75 GHz and (b) 7 GHz.

Excitation of the proposed antenna structure though the SubMiniature version A (SMA) connector's feed line can result in an imbalance in the current flow over the outer metallization

http://dx.doi.org/10.5772/66379

of the antenna, which can severely undermine the radiation characteristics of the antenna. To prevent this from happening, it was necessary to incorporate three smaller patches in the antenna slot. As is evident in **Figure 1**, only the middle patch is excited through the feed line, whereas the other two patches are used as parasitic radiators. This configuration facilitates the concentration of the EM fields in the proximity of the antenna structure instead of dispersing the field over its ground plane, which would otherwise contribute in unwanted coupling. **Figure 7** shows that a larger number of patches can significantly improve the antenna's bandwidth and gain properties. The antenna was implemented on a RT/duroid® RO4003 substrate with total dimensions of about 20 × 20 mm^2. Within this size, the maximum number of inner patch arms was restricted to three. The resulting antenna gain and radiation efficiency at its operating frequency range are given in **Table 1**.

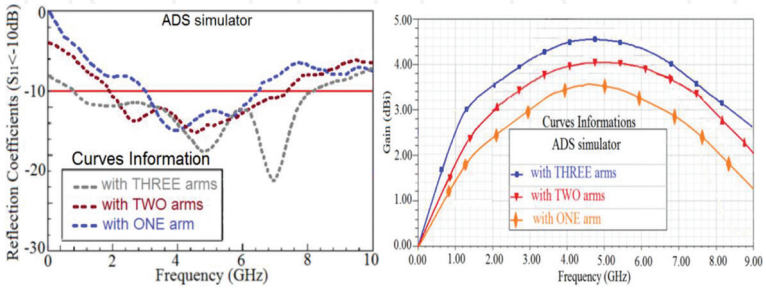

Figure 7. Simulated antenna reflection coefficient and gain response as a function of the number of inner patch arms.

Freq. (GHz)	Simulation (ADS)		Measured	
	Gain (dBi)	Efficiency (%)	Gain (dBi)	Efficiency (%)
0.70	1.8	53	1.2	50
4.75	4.6	82	4.0	80
7.00	3.7	75	3.6	73
8.00	3.1	70	3.1	68

Table 1. Antenna gain and radiation efficiency.

The radiation patterns of the antenna were simulated using ADS, CST-MWS and HFSS™. The simulated and measured radiation patterns are shown in **Figure 8** at the two resonance frequencies.

The antenna radiates similarly to a dipole antenna with a large coverage angle at the two resonance frequencies. **Figure 9** shows the simulated and measured radiation gains of the antenna. The measured radiation gain is greater than 1.2 dBi between 0.7 and 9 GHz, with a peak of 4.2 dBi at 4.8 GHz.

Table 2 shows comparison of the proposed antenna with similar antenna structures published in literature to date. It exhibits the largest fractional bandwidth and highest efficiency.

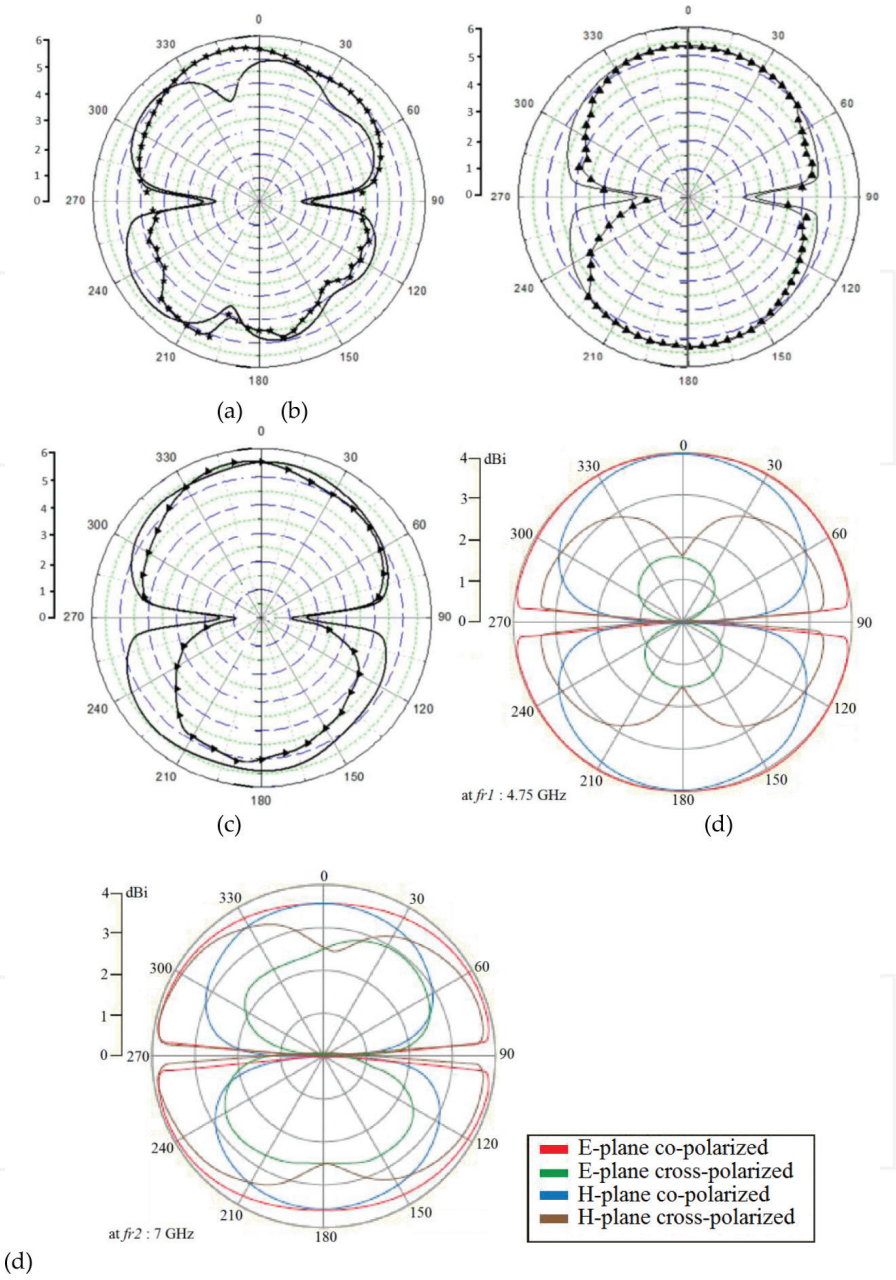

Figure 8. Simulated (E-plane) and measured (E-plane and H-plane) radiation patterns of the proposed antenna at the two resonance frequencies. (a) ADS at f_{r1} = 4.95 GHz (* line) and f_{r2} = 7.33 GHz (— line), (b) CST-MWS at f_{r1} = 4.03 GHz (▲ line) and f_{r2} = 6.68 GHz (— line), (c) HFSS at f_{r1} = 4 GHz (▲ line) and f_{r2} = 6.6 GHz (— line) and (d) measured at f_{r1} = 4.75 GHz and f_{r2} = 7 GHz.

http://dx.doi.org/10.5772/66379

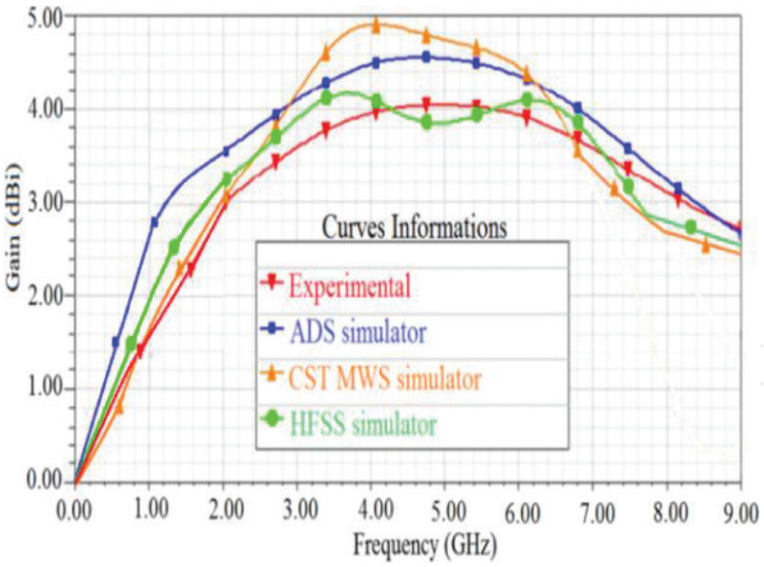

Figure 9. Antenna simulated and measured gain as a function of frequency.

Papers	Dimensions at 1 GHz	Bandwidth	Gain (max)	Eff. (max)
[2] 4 × UC antenna	0.047 λ_o × 0.021 λ_o × 0.002 λ_o 14.2 × 6.32 × 0.8 mm^3	104.8% (1–3.2 GHz)	2.3 dBi	62%
[2] 6 × UC antenna	0.064 λ_o × 0.021 λ_o × 0.0027 λ_o 19.2 × 6.32 × 0.8 mm^3	123.8% (0.8–3.4 GHz)	2.8 dBi	70%
[3] 5 × UC antenna	0.056 λ_o × 0.02 λ_o × 0.005λ_o 16.7 × 7 × 1.6 mm^3	82.9% (7.7–18.6 GHz)	3.1 dBi	58%
[3] 6 × UC antenna	0.06 λ_o × 0.02 λ_o × 0.027 λ_o 18 × 7 × 0.8 mm^3	74.4% (7.5–16.8 GHz)	2.1 dBi	44%
[3] 7 × UC antenna	0.072 λ_o × 0.02 λ_o × 0.005λ_o 21.7 × 7 × 1.6 mm^3	87.2% (7.8–19.85 GHz)	3.4 dBi	68%
[3] 8 × UC antenna	0.075 λ_o × 0.02 λ_o × 0.027 λ_o 22.6 × 7 × 0.8 mm^3	84.2% (7.25–17.8 GHz)	2.3 dBi	48%
[4]	0.2 λ_o × 0.05 λ_o × 0.003 λ_o 60 × 16 × 1 mm^3	116.7% (0.67–2.55 GHz)	4.74 dBi	62.9%
[5]	0.06 λ_o × 0.06 λ_o × 0.005 λ_o 18 × 18 × 1.6 mm^3	26.5% (1.8–2.35 GHz)	3.69 dBi	20%
[6]	0.2 λ_o × 0.017λ_o × 0.017λ_o 60 × 5 × 5 mm^3	103% (0.8–2.5 GHz)	0.45 dBi	53.6%
[7]	0.06λ_o ×0.06λ_o ×0.021λ_o 18.2×18.2×6.5 mm^3	66.7% (1–2 GHz)	0.6 dBi	26%
[8]	0.04λ_o ×0.04λ_o ×0.011λ_o 12×12×3.33 mm^3	8.2% (2.34–2.54 GHz)	1 dBi	22%
[9]	0.07λ_o×0.08λ_o×0.003λ_o 20×25×0.8 mm^3	8.3% (3.45–3.75 GHz)	2 dBi	27%
Proposed antenna	0.072λ_o×0.066λ_o×0.002λ_o 21.6×19.8×0.8 mm^3	167.8% (0.7–8 GHz)	4 dBi	80%

Table 2. Antenna performance compared to other miniature UWB antennas (UC: Unit Cell).

It has the second highest gain and its relatively small size is comparable to most previous works. These results clearly confirm that the antenna is great candidate for ultra-wideband communication systems.

2.1. Effect of the 50-Ω load on the antenna bandwidth

The return loss of the antenna with and without the 50-Ω load is shown in **Figure 10**. It is evident that the 50-Ω load enhances the impedance match so that the impedance bandwidth improves from 131.8% (without 50 Ω) up to 164.6% (with 50 Ω). Excellent match is discerned near the two resonance frequencies of the antenna, at 4.8 and 7 GHz, thus enabling effective radiation at the resonance frequencies. These results are summarized in **Table 3**.

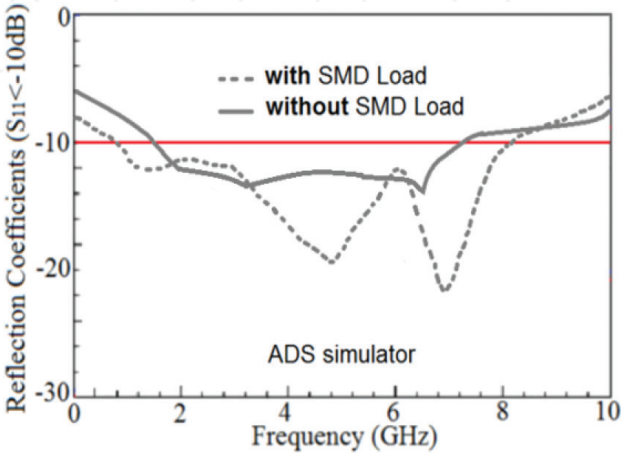

Figure 10. Antenna reflection coefficient (S_{11}) as a function of frequency with and without a 50-Ω load.

Unloaded	1.5–7.3 GHz, Δf = 5.8 GHz ≈ 131.8%
Loaded	0.8–8.24 GHz, Δf = 7.44 GHz ≈ 164.6%

Table 3. Antenna bandwidth with and without 50-Ω load.

2.2. Effect of the SMD load on the radiation performance

Antenna gain and efficiency performance, with and without the 50-Ω impedance load, are shown in **Figure 11**, and the results are tabulated in **Table 4**. These results show that a small improvement is achieved with loading the antenna.

http://dx.doi.org/10.5772/66379

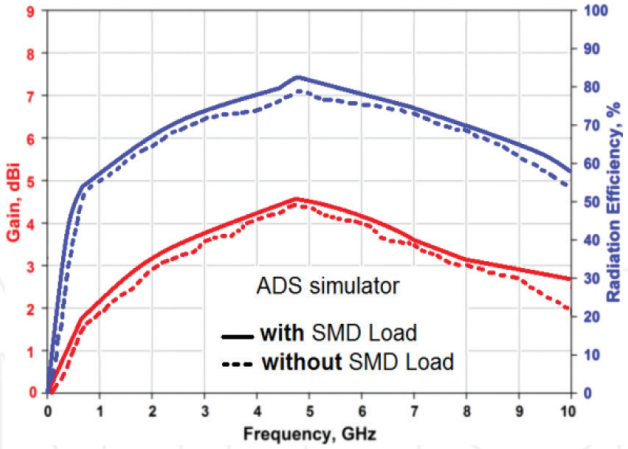

Figure 11. Antenna gain and efficiency with and without 50-Ω impedance loading simulated as a function of frequency.

Unloaded				
Frequency (GHz)	0.7	4.75	7	8
Gain (dBi)	1.6	4.5	3.6	3
Efficiency (%)	51	79	73	69
Loaded				
Frequency (GHz)	0.7	4.75	7	8
Gain (dBi)	1.8	4.6	3.7	3.1
Efficiency (%)	53	82	75	70

Table 4. Radiation properties unloaded/loaded by 50 Ω.

3. Hexa-band antenna

Configuration of a novel hexa-band CPW-fed antenna, shown in **Figure 12**, comprises three asymmetric fork-shaped-radiating stubs with U-shaped-radiating elements. Embedded within the U-shaped elements is a dielectric slit. The tri-branched radiator generates three distinct resonant frequencies within the L-, S-, C- and X-bands. The U-shaped element also generates resonant frequencies at the lower band of the antenna. The asymmetrical fork-shaped stubs improve the impedance-matching characteristics of the antenna and reduce its stopband. The antenna is fabricated on an FR4 substrate with relative permittivity $\varepsilon_r = 4.4$ and thickness $h = 1.6$ mm and is fed through a coplanar waveguide transmission line with 50-Ω impedance. The substrate size is 35×26 mm^2.

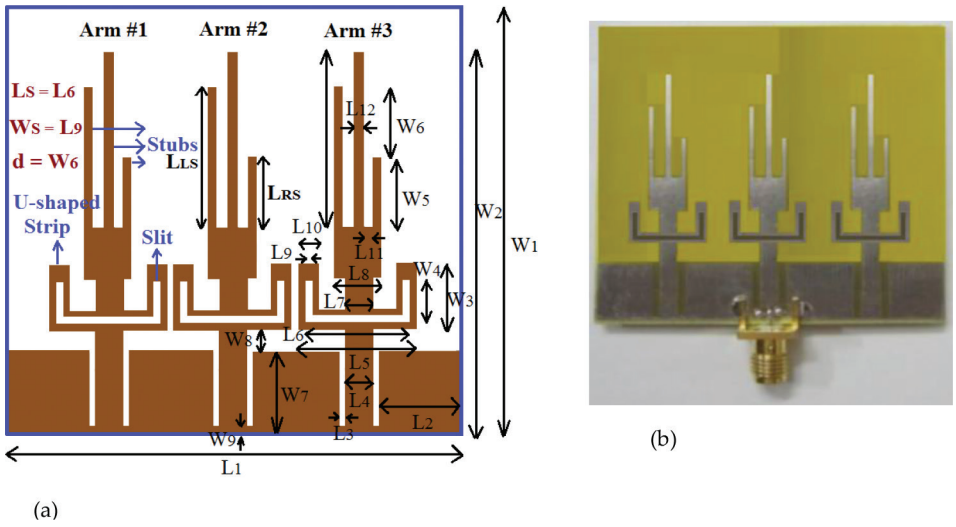

Figure 12. CPW-fed monopole hexa-band antenna: (a) top view of the proposed antenna and (b) the fabricated antenna.

The antenna was excited through a 50-Ω coplanar waveguide transmission line. **Figure 13** shows that it resonates at 1.3, 1.75, 3.35, 4.85, 6.5 and 7.6 GHz. There is good agreement between simulated and measured results. Any divergence between the simulated and measured results is ascribed to a number of factors, that is (1) the non-uniform current density distribution over the antenna structure, (ii) imperfect equivalent circuit models, (iii) undesirable EM coupling and (iv) manufacturing errors. This antenna is shown to function between 700 MHz and 11.35 GHz, and has a fractional bandwidth of 176.76% that includes several communication standards, in particular, GSM, DCS, PCS, Bluetooth, WLAN, WiMAX and WiFi along with the major parts of the C- and X-bands. The measured E-plane and H-plane radiation characteristics at 1.3, 1.75, 3.35, 4.85, 6.5 and 7.6 GHz are shown in **Figure 14**. The measured results show that the antenna radiates omnidirectionally at these frequencies.

In **Figure 13**, the impedance bandwidth of the lower passband at 1.3 GHz is 800 MHz (0.7–1.5 GHz) with a corresponding fractional bandwidth of 72.72%. The impedance bandwidth of the next passband at 1.75 GHz is 1100 MHz (1.6–2.7 GHz) with S_{11} better than 15 dB and functions at GSM (upper), DCS, PCS, WiFi (lower), Bluetooth, WiMAX (lower) and WLAN (2.4–2.484 GHz). The impedance bandwidth of the passband at 3.35 GHz is 1.75 GHz (2.85–4.6 GHz) covering the WiMAX (upper) band. The subsequent passbands at 4.85 GHz, at 6.5 GHz and at 7.6 GHz have impedance bandwidths of 1.35 GHz (4.65–6 GHz), 0.95 GHz (6.25–7.2 GHz) and 4 GHz (7.35–11.35 GHz), respectively, covering WiFi (upper) band and significant parts of C- and X-bands. The impedance bandwidth, passband and stopband of antenna-I are given in **Table 5**.

http://dx.doi.org/10.5772/66379

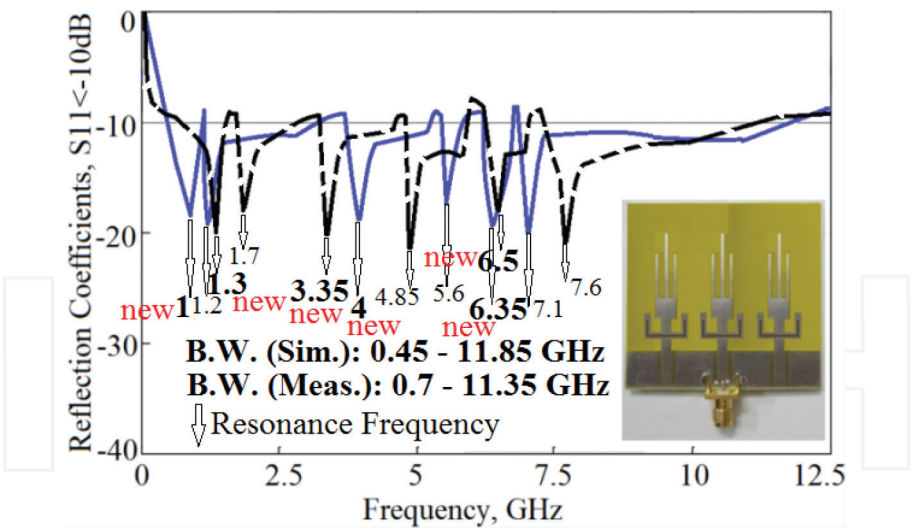

Figure 13. Simulated (solid-line) and measured (dashed-line) S_{11} response of the antenna.

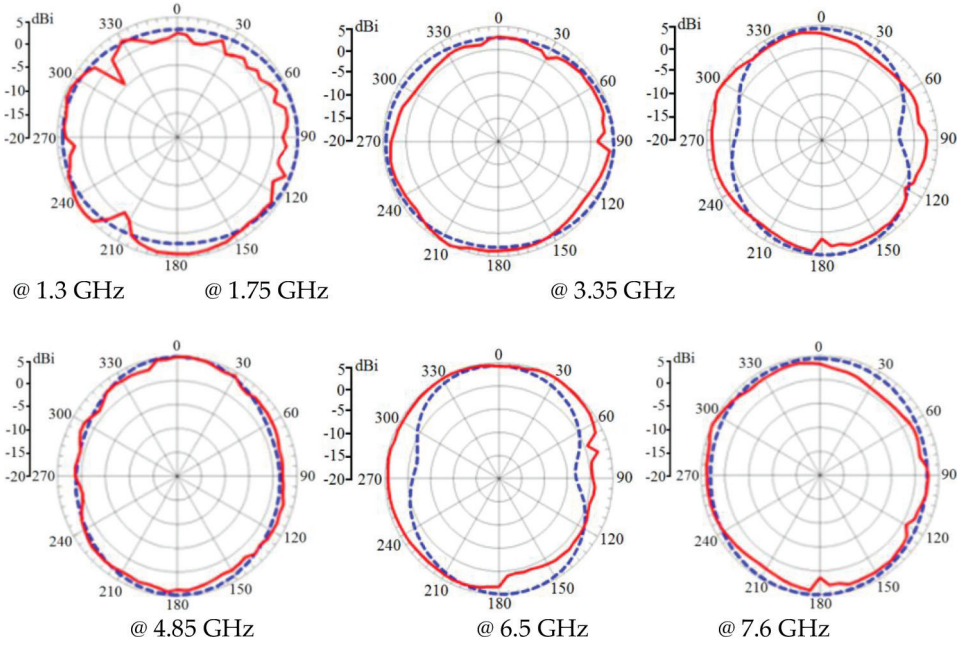

Figure 14. Measured E-plane (dashed-line) and H-plane (solid-line) radiation patterns of the antenna at the resonance frequencies.

Total Imp. BW	**176.76% (0.7–11.35 GHz)**
Passband 1	72.72% (0.7–1.5 GHz) → f_{r1} =1.3 GHz
Stopband 1	1.51–1.59 GHz
Passband 2	51.16% (1.6–2.7 GHz) → f_{r2} =1.75 GHz
Stopband 2	2.71–2.84 GHz
Passband 3	46.97% (2.85–4.6 GHz) → f_{r3} =3.35 GHz
Stopband 3	4.61–4.64 GHz
Passband 4	25.35% (4.65–6 GHz) → f_{r4} =4.85 GHz
Stopband 4	6.01–6.24 GHz
Passband 5	14.12% (6.25–7.2 GHz) → f_{r5} =6.5 GHz
Stopband 5	7.21–7.34 GHz
Passband 6	42.78% (7.35–11.35GHz) → f_{r6} =7.6GHz

Table 5. Impedance bandwidth of the antenna (f_{rN}: resonance frequency of band N).

Table 6 shows a comparison of the proposed antenna with similar antennas published in literature. Parameters compared are (i) the number of distinct bands, (ii) the communication standards being covered and (iii) the sizes of the antennas. It is evident that the proposed antenna operates in the following communication bands: GSM (880–960 MHz/1.85–1.99 GHz), DCS (1.71–1.88 GHz), PCS (1.71–1.99 GHz), Bluetooth (2.402–2.480 GHz), WLAN (2.4/5.2/5.8 GHz), WiMAX (2.3–2.4/2.496–2.690/3.3–3.8 GHz), WiFi (2.412–2.4835/4.9–5.9 GHz) and parts of the C- and X-bands. The antenna provides substantially greater coverage than other antennas reported in Refs. [9, 10, 14, 15]. Dimensions of the proposed antenna are comparable to other antennas.

Multiband antennas	**Proposed antenna**	**[9]**	**[10]**	**[11]**	**[12]**	**[13]**	**[14]**	**[15]**
Number of separated bands	6	3	3	3	4	3	2	2
Coverage bands								
C-band	√	–	–	–	–	–	–	√
X-band	√	–	–	–	–	–	–	–
WiMAX	√	√	–	–	√	√	–	–
Bluetooth	√	–	–	–	–	√	–	–
WLAN	√	√	–	–	√	–	√	√
WiFi	√	–	√	√	√	√	–	–
PCS	√	–	–	–	–	–	√	–
DCS	√	–	√	√	–	–	–	–
GSM	√	–	–	–	–	–	–	–
Max. gain (dBi)	5.3	3.06	2.57	3.6	5.0	6.7	5.5	5.2
Dimensions (mm^2)	35 × 26	32 × 28	25 × 38	20 × 20	44 × 56	50 × 50	54 × 52	32.5 × 25

Table 6. Characteristics of the antenna in comparison with recent work.

http://dx.doi.org/10.5772/66379

4. Conclusion

To summarize, a compact antenna comprising three asymmetrical branched fork with U-shaped strips is shown to exhibit hexa-band characteristics. The antenna meets multi-communication standards including L-, S-, C- and X-bands for GSM, DCS, PCS, Bluetooth, WLAN, WiMAX and WiFi applications. Slits in the U-shaped strips are shown to excite additional resonant bands. The proposed structure reduces stopbands and improves the antenna's impedance-matching performance. The antenna exhibits good return loss, gain and radiation patterns, which makes it an excellent candidate for multiband and broadband communication applications.

Acknowledgements

The Authors would like to give their special thanks to faculty of microelectronics for the financial support.

Author details

Mohammad Alibakhshikenari[1]*, Mohammad Naser-Moghadasi[2], Ramazan Ali Sadeghzadeh[3], Bal Singh Virdee[4] and Ernesto Limiti[1]

*Address all correspondence to: Alibakhshikenari@ing.uniroma2.it

1 Department of Electronic Engineering, University of Rome Tor Vergata, Rome, Italy

2 Faculty of Engineering, Science and Research Branch, Islamic Azad University, Tehran, Iran

3 Faculty of Electrical Engineering, K. N. Toosi University of Technology, Tehran, Iran

4 London Metropolitan University, Center for Communications Technology, London, UK

References

[1] X.Q. Lin, R.P. Liu, X.M. Yang, J.X. Chen, X.X. Ying, Q. Cheng, "Arbitrarily dual-band components using simplified structures of conventional CRLH TLs," *IEEE Transactions on Microwave Theory and Techniques*, 2006; 54(7): 2902–2909. DOI: 10.1109/TMTT.2006.877434

[2] M. Alibakhshi-Kenari, "Printed planar patch antennas based on metamaterial," *International Journal of Electronics Letters* 2014;2(1):37–42. DOI: 10.1080/21681724.2013.874042

[3] M. Alibakhshi-Kenari, "Introducing the new wideband small plate antennas with engraved voids to form new geometries based on CRLH MTM-TLs for wireless applications", *International Journal of Microwave and Wireless Technologies*, 2014;6(06):629-637.

[4] J. Luo, S. Gong, P. Duan, C. Mou, M. Long, "Small-size wideband monopole antenna with CRLH-TL for LTE mobile phone," *Progress in Electromagnetics Research C*, 2014;50:171–179.

[5] M.A. Abdalla, A.A. Awad, K.M. Hassan, "Wide band high selective compact metamaterial antenna for 2 GHz Wireless applications," *Antennas and Propagation Conf. (LAPC)*, 2014:350–354.

[6] Y. Li, Z. Zhang, J. Zheng, Z. Feng, "Compact heptaband reconfigurable loop antenna for mobile handset," *IEEE Antennas and Wireless Propagation Letters*, 2011;10:1162–1165.DOI: 10.1109/LAWP.2011.2171311

[7] C.J. Lee, K.M.K.H. Leong, T. Itoh, "Composite right/left-handed transmission line based compact resonant antennas for RF module integration," *IEEE Transactions on Antennas Propagation*, 2006; 54(8): 2283–2291. DOI: 10.1109/TAP.2006.879199

[8] C.-C. Yu, M.-H. Huang, L.-K. Lin, Y.-T. Chang, "A compact antenna based on MTM for WiMAX," *Asia-Pacific Microwave Conference (APMC),* 2008; 2: 1127–1130.

[9] W. Hu, Y.-Z. Yin, P. Fei, X. Yang, "Compact triband square-slot antenna with symmetrical L-strips for WLAN/WiMAX applications," *IEEE Antennas Wireless Propagation Letter*, 2011; 10: 462–465. DOI: 10.1109/LAWP.2011.2154372

[10] J. Pei, A.-G. Wang, S. Gao, W. Leng, "Miniaturized triple-band antenna with a defected ground plane for WLAN/WiMAX applications," *IEEE Antennas Wireless Propagation Letter*, 2011; 10: 298–301. DOI: 10.1109/LAWP.2011.2140090

[11] N. Amani, M. Kamyab, A. Jafargholi, A. Hosseinbeig, J.S. Meiguni, "Compact tri-band metamaterial-inspired antenna based on CRLH resonant structures," *Electronics Letters*, 2014; 50(12): 847–848. DOI: 10.1049/el.2014.0875

[12] Y.F. Cao, S.W. Cheung, T.I. Yuk, "A multiband slot antenna for GPS/WiMAX/WLAN systems," *IEEE Transactions on Antennas and Propagation*, 2015; 63(3): 959–958. DOI: 10.1109/TAP.2015.2389219

[13] V.V. Reddy, N.V.S.N. Sarma, "Triband circularly polarized Koch fractal boundary microstrip antenna," *IEEE Antennas and Wireless Propagation Letters*, 2014; 13: 1057–1060. DOI: 10.1109/LAWP.2014.2327566

[14] C. Wang, Z.-H. Yan, P. Xu, J.-B. Jiang, B. Li, "Trident-shaped dual-band CPW-fed monopole antenna for PCS/WLAN applications," *Electronics Letters*, 2011; 47(4): 231–232. DOI: 10.1049/el.2010.3250

[15] X. Yang, Y.Z. Yin, W. Hu, K. Song, "Dual-band planar monopole antenna loaded with pair of edge resonators," *Electronics Letters*, 2010; 46(21): 1419–1421. DOI: 10.1049/el.2010.8349